Physics of Fluids ARTICLE scitation.org/journal/phf

Effect of the aspect ratio on the dynamics of air bubbles within Rayleigh–Bénard convection

Cite as: Phys. Fluids **33**, 095104 (2021); doi: 10.1063/5.0060148
Submitted: 15 June 2021 · Accepted: 20 August 2021 ·
Published Online: 2 September 2021

Jin-Tae Kim (김진태),[1] Yongsang Kim (김용상),[2] Soohyeon Kang (강수현),[3] Jaewook Nam (남재욱),[2] Changhoon Lee (이창훈),[4,5] and Leonardo P. Chamorro[6,7,8,9,a)]

AFFILIATIONS

[1]Querrey Simpson Institute for Bioelectronics, Northwestern University, Evanston, Illinois 60208, USA
[2]School of Mathematics and Computing, Yonsei University, Seoul 03722, South Korea
[3]Mechanical Science and Engineering, University of Illinois, Urbana, Illinois 61801, USA
[4]School of Mathematics and Computing, Yonsei University, Seoul 03722, South Korea
[5]Department of Mechanical Engineering, Yonsei University, Seoul 03722, South Korea
[6]Department of Mechanical Science and Engineering, University of Illinois, Urbana, Illinois 61801, USA
[7]Department of Aerospace Engineering, University of Illinois, Urbana, Illinois 61801, USA
[8]Department of Civil and Environmental Engineering, University of Illinois, Urbana, Illinois 61801, USA
[9]Department of Geology, University of Illinois, Urbana, Illinois 61801, USA

Note: This paper is part of the special topic, Tribute to Frank M. White on his 88th Anniversary.
[a)]**Author to whom correspondence should be addressed:** lpchamo@illinois.edu

ABSTRACT

Laboratory experiments and numerical simulations were performed to quantify the effect of the aspect ratio, Γ, in the dynamics of air bubbles within turbulent Rayleigh–Bénard (RB) convection. We explored four scenarios defined by $\Gamma = 1.25$, 1.5, 2, and 2.5 under Rayleigh numbers ranging from 2.0×10^9 to 1.6×10^{10}. Continuous 1-mm bubbles were released at two locations from the bottom along the roll path. Three-dimensional particle tracking velocimetry was used to track a large number of bubbles and determine features of the trajectories and pair dispersion, $R^2(t)$, for various initial separations, r_p within $H/10 \leq r_p \leq 5H/10$; here, H is the height. The $R^2(t)$ of the bubbles within a quiescent medium was included for reference. Characterization of the bubble streams, namely, the center of mass (L_c), mean deviation (R_c) to L_c, vertical (v_z) and lateral (v_L) velocities, and their ratios reveal the strong modulation of the roll structure and Γ. In particular, L_c exhibited an approximately symmetric distribution around the maximum, which occurred at the middle height only in the $\Gamma = 1.25$ case. Maximum L_c was near the wall top with the highest aspect ratio. However, R_c did not vary substantially among the cases. Bubbles' lateral pair dispersion R_L^2 shows correlated trends with Γ, particularly at large initial separations and times, whereas the vertical pair dispersion is mainly dominated by buoyancy. The R_L^2 decreased as Γ increased. It indicates the effect of different-sized roll structures modulated by Γ. In general, R^2 embodies distinct features of Γ-modulated bubble dynamics in RB convection.

I. INTRODUCTION

Rayleigh–Bénard (RB) convection is a fundamental phenomenon that finds many applications in environmental physics and engineering systems.[1] Many buoyancy-driven flows usually contain inertial particles, namely, contaminants in the atmosphere, water droplets in clouds, bubbles and plankton in the oceans, and fuel sprays in engine combustion.[2] There, inertial particles play a crucial role in transporting, e.g., nutrients or chemicals. Their dynamics can be quantified by considering the so-called pair dispersion $R^2 = \langle [r_p(t) - r]^2 \rangle$, where $\langle\rangle$ is the averaging operator, $r_p(t)$ is the distance between two-particle trajectories as a function of time, and r is the initial separation (e.g., Ref. 3). Lagrangian models that describe the flow properties in terms of variables defined at the reference frame of individual fluid particles carried by the flow are required to characterize pair dispersion.[2]

Substantial effort has been placed in describing Lagrangian dynamics of convective turbulence. Associated Lagrangian statistics are different from that of homogeneous isotropic turbulence; the flow inhomogeneity and large-scale circulation of dominant roll motions

affect Lagrangian statistics in turbulent convection.[4,5] Most of the studies have focused on uncovering the physics of the induced flow (e.g., Refs. 6–10); scenarios containing inertial particles that are an intrinsic component of natural and engineering systems remain obscure.[11] Inertial particles detach from fluid paths and distribute inhomogeneously.[12–15] Air bubbles are a special case of inertial particles. Density difference from the fluid carrier causes path and wake instability; air bubbles in homogeneous and isotropic turbulent flows disperse faster than tracers, exhibiting ballistic-to-diffusion (t^2 to t^1) transition.[15] In a previous work,[11] the Lagrangian dynamics of air bubbles in RB convection was investigated and found that air-bubbles R^2 near the center of a convective cell exhibited ballistic-to-diffusion transition, which is similar to the case of isotropic turbulence with tracer particles.[10] However, this quantity showed a $t^{3/2}$ power-law behavior away from the center due to RB convection's inhomogeneity and anisotropy. The path instability of the bubbles showed that the medium suppressed the bubbles' wake-induced motion, resulting in a reduction of the bubbles' lateral velocity.

Despite the remarkable progress made to understand RB convection, there is a large gap in quantifying associated phenomena with inertial particles and the role of other quantities, including geometry. Aspect ratio Γ, defined as a ratio of the side length L to the height H of the domain, is one of the important parameters that modulate the flow and heat transfer dynamics. Bailon-Cuba *et al.*[16] explored numerically the aspect ratio dependence within $0.25 \leq \Gamma \leq 12$ on the heat transfer in a cylindrical cell for Rayleigh numbers $10^7 \leq Ra \leq 10^9$ and Prandtl numbers $Pr = 0.7$. They noted a local minimum of the heat transfer at $\Gamma \approx 2.5$ with a transition from a single-roll to a double-roll structure. Huang *et al.*[17] experimentally and numerically studied the effect of spatial confinement in convective turbulence. They found that as the width of the convection cell is narrowed, the heat-transfer efficiency significantly increases due to the changes in the dynamics of thermal plumes in the boundary layers and large-scale flows. Recently, Huang *et al.*[18] numerically investigated the influence of the aspect ratio within $1/60 \leq \Gamma \leq 1$ on the dynamics of thermal plumes in a box-shaped container at $Ra = 10^9$ and $Pr = 11.57$. They observed thermal plumes mainly near the container's sidewalls at relatively large aspect ratios and more plumes at the center of the container at small aspect ratios.

Experiments in cylindrical-[19] and rectangular-shaped containers[20,21] have noted the cessation and reversal of large-scale circulation affected by the aspect ratio. In general, geometry plays an important role in determining the dominant flow structures; it may also influence the Lagrangian dynamics of inertial particles in RB convection. Here, we investigated the dynamics of air bubbles in RB convection at four aspect ratios $\Gamma = 1.25$, 1.5, 2, and 2.5 using experiments and numerical simulations. We quantified the Lagrangian properties of bubble motions using 3D particle tracking velocimetry (3D-PTV) and described the flow and inspected bubble dynamics with numerical simulations.

II. APPROACH

A. Laboratory experiments

Experiments were conducted in a box-shaped container with a square cross section of $L = W = 500$ mm; the height H of the RB box is varied to produce various aspect ratios $\Gamma = 1.25$, 1.5, 2, and 2.5. The tank walls are made of double-pane insulated tempered 3.175 mm thick glass panels separated by a 9.5 mm barrier of inert gas. The tank's base has an 800 W, 457.2 mm × 457.2 mm flat silicone heater, adhered to an 11 mm thick aluminum plate. To further prevent heat leakage, the bottom side of the heating element is aligned with a high-temperature patterned silicone matte layer. A temperature sensor was set in contact with the heating element. A cooling aluminum plate was placed at the top of the tank with adjustable hanging height and connected to a 1000 W capacity PolyScience refrigerated circulator. Insulating foam panels were also attached to the top and sidewalls; see additional details in Ref. 8.

The RB tank was filled with de-ionized water, which resulted in the Prandtl number of $Pr = \nu/\kappa \approx 5.4$. The various convective flows were induced with a temperature difference $\Delta T = 10\,^{\circ}\mathrm{C}$, resulting in Nusselt numbers $Nu = QH/\lambda\Delta T$ ranging from 100 to 200 and Rayleigh numbers $Ra = g\alpha\Delta T H^3/\kappa\nu$ ranging from 2.0×10^9 to 1.6×10^{10} for the different aspect ratios. Here, ν is the kinematic viscosity, κ is the thermal diffusivity, λ is the thermal conductivity, α is the thermal expansion coefficient of the fluid, Q is the heat flux across the cell, and g is the gravitational acceleration. The bulk dissipation rate was estimated as $\langle\varepsilon\rangle = RaPr^{-2}(Nu-1)\nu^3/H^4$, which shows similar values of about 2.28×10^{-6} m^2 s^{-3} for all Γ. The corresponding Kolmogorov length scale was $\eta = (\nu^3/\langle\varepsilon\rangle)^{1/4} \approx 6.9 \times 10^{-4}$ m, and the timescale was $\tau = \sqrt{\nu/\langle\varepsilon\rangle} \approx 0.6$ s, see basic parameters in Table I.

Air-bubble streams were formed using two porous stones connected to a 4 W air pump. The bubble generator was placed at $s/D = -1/2$ and 1/2, where s is the distance along the base diagonal with origin at the center, and $D = 283$ mm is the diagonal half length of the RB tank. Bubbles of diameter $d_b = 0.96 \pm 0,15$ mm $(1.4\eta \pm 0.2\eta)$ were released in a single column at a rate of 10.7 bubbles s^{-1}; their bulk rising velocity in a quiescent medium was $u_b \approx 0.09$ m s^{-1}. The bubble volume fraction ϕ_v was about 1×10^{-6}, and the surface fraction ϕ_s was about 5×10^{-4}, resulting in negligible effects on the flow.[22]

TABLE I. RB cases—basic quantities. H: height; Γ: aspect ratio; Ra: Rayleigh number; Nu: Nusselt number; $\langle\epsilon\rangle$, τ, and η: Kolmogorov's dissipation rate, time, and length scales, respectively.

H (mm)	Γ (–)	Ra (–)	Nu (–)	$\langle\varepsilon\rangle$ (m^2 s^{-3})	τ (s)	η (m)
400	1.25	1.61	2.08×10^2	2.28×10^{-6}	5.93×10^{-1}	6.89×10^{-4}
333	1.5	9.26×10^9	1.73×10^2	2.28×10^{-6}	5.93×10^{-1}	6.89×10^{-4}
250	2.0	3.92×10^9	1.30×10^2	2.27×10^{-6}	5.93×10^{-1}	6.89×10^{-4}
200	2.5	2.01×10^9	1.04×10^2	2.27×10^{-6}	5.94×10^{-1}	6.90×10^{-4}

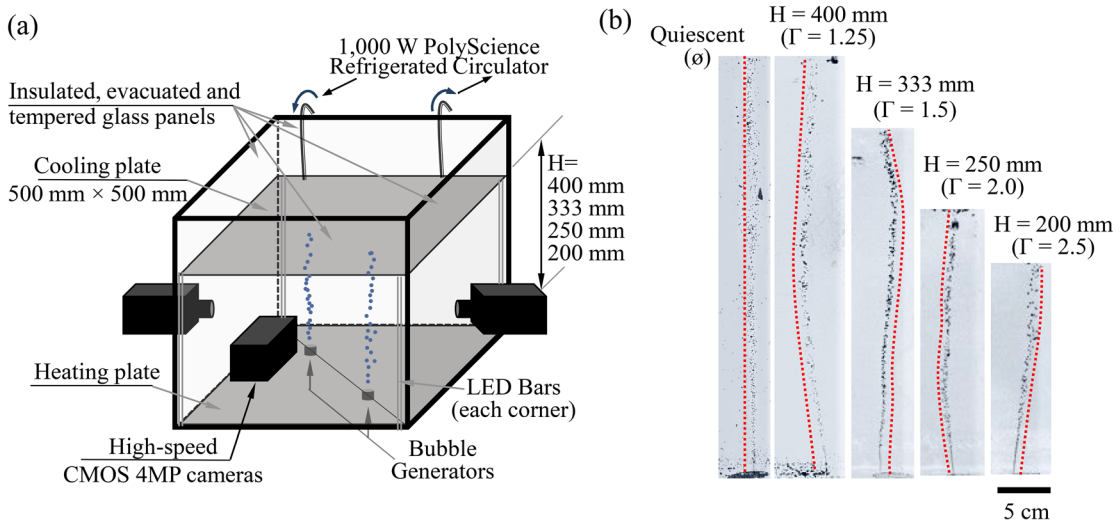

FIG. 1. (a) Basic schematic highlighting the bubble streams at $s/D = -1/2$ and 1/2; s is the coordinate along the diagonal, D, with origin at the center. (b) Photographs of bubbles' paths at various Γ; the quiescent medium case is included for reference. The yellow lines highlight the bulk path features.

Three high-speed, CMOS 4MP (2048 pixels × 2048 pixels) cameras were mounted on three lateral walls of the tank to track the bubbles' 3D trajectories, see schematics in Fig. 1. LED light bars were placed in each corner of the box to illuminate the bubbles. Each camera covered an investigation region of $L/2 \times H$, and thus, the total investigation volume was $L/2 \times L/2 \times H$. The flow was left to develop for at least 30 min to allow stable RB convection before using the bubble generator. The bubbles on the top plate were removed before each measurement to minimize local effects on the top. We tracked the bubbles 10 s after the release to minimize transient effects. For each case, 1800 consecutive three-view-image sets were obtained at a sampling rate of 200 Hz, which allowed a description of the trajectories at the sub-Kolmogorov timescale. The air bubbles were tracked using a three-dimensional particle tracking velocimetry (3D PTV), where a 3D calibration used a planar target placed at multiple locations.[8] The pixel-to-distance ratio was ∼ 0.18 mm/pixel, and the root mean square of the difference between reconstructed and true calibration points was on the order of 10^{-2} mm. For each scenario, approximately 5×10^3 trajectories with an average of 122 frames and 5.5×10^5 data samples were tracked using the Hungarian algorithm,[23] which were linked using a three-frame gap closing for long trajectories reconstruction. Nearly 300 bubbles were followed simultaneously, allowing for the characterization of various initial separations. Bubble trajectories and temporal derivatives were estimated using fourth-order B splines, see additional details of the 3D-PTV setup in Ref. 11.

B. Numerical simulations

Complementary numerical simulations of Rayleigh–Bénard Convection under the same experimental conditions were performed by solving the Navier–Stokes' energy and continuity equations under the Boussinesq approximation, given as follows:

$$\frac{\partial u_i}{\partial t} + \frac{\partial u_i u_j}{\partial x_j} = -\frac{1}{\rho}\frac{\partial p}{\partial x_i} + \nu\frac{\partial^2 u_i}{\partial x_j^2} + g\beta T\delta_{i2}, \tag{1}$$

$$\frac{\partial T}{\partial t} + \frac{\partial u_j T}{\partial x_j} = \kappa\frac{\partial^2 T}{\partial x_j^2}, \text{ and } \frac{\partial u_j}{\partial x_j} = 0. \tag{2}$$

Here, u_i is the i-component of the flow velocity, t is the time, ρ is the fluid density, p is the pressure, β is the thermal expansion coefficient, and δ_{ij} is the Kronecker operator.

A second-order central difference scheme was used to approximate the spatial terms, and a third-order hybrid Runge-Kutta method[24] was used for the temporal advancement. The Poisson equation for decoupled pressure was solved directly by using a discrete cosine transform. A quick scheme was applied in the energy equation to satisfy the conservation of the passive scalar term. The boundary conditions included no-slip, $u_i|_\partial = 0$, at the walls, adiabatic conditions, $\frac{\partial T}{\partial x_i}|_\partial = 0$, on sidewalls, and constant temperature on the top and bottom walls. Numerical simulations were performed with a uniform grid in the horizontal directions and a hyperbolic tangent grid in the vertical direction at a resolution of 256 × 256 × 128 grids in all the scenarios. A non-uniform grid was adopted to capture steep variations of temperature and momentum in the boundary layer's vicinity; the ratio of the horizontal grid range to the vertical grid range is changed from 1 to 0.4 as the aspect ratio changed from Γ = 1 to 2.5. The corresponding grid size relative to the averaged Kolmogorov length scale is $\Delta x/\eta \simeq 2$ and $\Delta z_{min}/\eta \simeq 0.3$–0.6. Given that the Batchelor scale is roughly 1/2 of the Kolmogorov scale, our grid seems marginal. More importantly, the small-scale behavior near the bottom and top walls, where the major heat transfer occurs, needs to be properly resolved. Using a non-uniform grid there, we maintained $\Delta z_{min}/\eta_{min} \simeq 1.0$–2.0, where η_{min} is the minimum local Kolmogorov length scale that is about 1/3 of the averaged Kolmogorov length scale η. The momentum and thermal boundary layer thicknesses near the bottom wall are found in the range of 20–30 mm, and at least 20 wall-normal grids were used to resolve steep variations. Therefore, as we showed in our previous work,[11] the resolution test with higher resolutions did not make meaningful difference. Furthermore, the validation with the same grids for a similar problem

clearly indicated good agreement against the measurements, as discussed in Ref. 11; it also includes details on the validation of the simulations and application to a similar problem.

The point-particle approximation is one of the methods used to describe the behavior of particle-laden flows. Various studies (e.g., Refs. 25–27) have shown that bubble motions are primarily determined by gravity, lift and drag forces, added mass, and fluid acceleration. By assuming that the bubbles have a roughly spherical shape and neglecting finite Reynolds number corrections, the bubbles' motions may be described by

$$\frac{dv_i}{dt} = 3\frac{Du_i}{Dt} - \frac{1}{\tau_b}(v_i - u_i) - 2g\delta_{i2} - \varepsilon_{ijk}(v_j - u_j)\omega_k$$
$$\text{and } \frac{dx_i}{dt} = v_i, \tag{3}$$

where x_i and v_i are the bubbles position and velocity, respectively, ω_i is the flow vorticity, ε_{ijk} is the permutation tensor, and $\tau_b = d_b^2/24\nu$ is the bubble timescale. A fourth-order Hermite interpolation scheme is used to estimate the bubble's velocity and flow vorticity at any time. The bubbles' initial velocity was set to as local fluid flow velocity. We used the one-way coupling approximation; then, there is no additional force exerted by the bubble motion. A total of 625 bubbles were released for each scenario. The major limitation of the current modeling of the bubble motion is that it is valid only for bubbles much smaller than the Kolmogorov length scale. Although the bubble size is comparable with the Kolmogorov length scale in the current experimental settings, the point-particle modeling is believed to capture the main dynamics of bubbles in turbulence, as shown in the comparison of the statistics of bubbles such as the RMS velocity between the experiment and simulations. Also, we did not consider the two-way coupling between the bubbles and turbulence in our simulations although the bubble density is relatively concentrated along the bubble path in the experiment. As shown in a recent simulation study on the two-way coupling between bubbles and turbulence,[28] the modification of turbulence by rising bubbles is quite minimal in terms of various statistics. Therefore, we concluded that the two-way effect is negligible.

III. DISCUSSION

A first, qualitative inspection into the effect of Γ on the features of the rising bubble streams is shown in Fig. 2(a) with superimposed 3D trajectories. There, the colored trajectories representing the y-axis velocity component are included to aid insight. The case with a quiescent scenario is also included to illustrate the modulation of the various RB convection scenarios. The bubbles dispersed approximately homogeneously in the lateral direction in the quiescent medium as they rose around the vertical axis crossing $s/D = 1/2$. However, in the convective flows, the dominant roll structures modulated by the aspect ratio Γ induced distinct curved trajectories deviating from the vertical path. It is also worth pointing out that the normalized lateral velocity component, $u_L\tau/\eta$, exhibits distinct distribution affected by Γ, whereas this quantity is approximately uniform in the quiescent case. The time history of the bubbles reaching the vicinity of the top wall shown in Fig. 2(b) reveals the additional effect of Γ in the convection. Note that the distribution of the bubbles is around the relative $(x_0, y_0) = (0, 0)$ only in the quiescent scenario. Irregular distributions of the (x_0, y_0) are dominant in the convective cases. Quantification of such features along the vertical path is discussed later.

Basic assessment of the characteristics of the background flows induced by the RB convection at $\Gamma = 1.25$, 1.5, 2, and 2.5 is given in Fig. 3 with the numerical simulations of the in-plane velocity u_L and associated standard deviations, σ_{uL}, in the vertical plane coincident with the box diagonal and motion of the roll convection cell. They show that the flow structure does not change significantly with the aspect ratio. However, the standard deviation of the velocity fluctuations undergoes a monotonic increase around the center with an increase in the aspect ratio. Bailon-Cuba *et al.*[16] noted a transition to the double roll structure at $\Gamma \geq 2.5$, which defined an upper bound of the exploratory cases studied here.

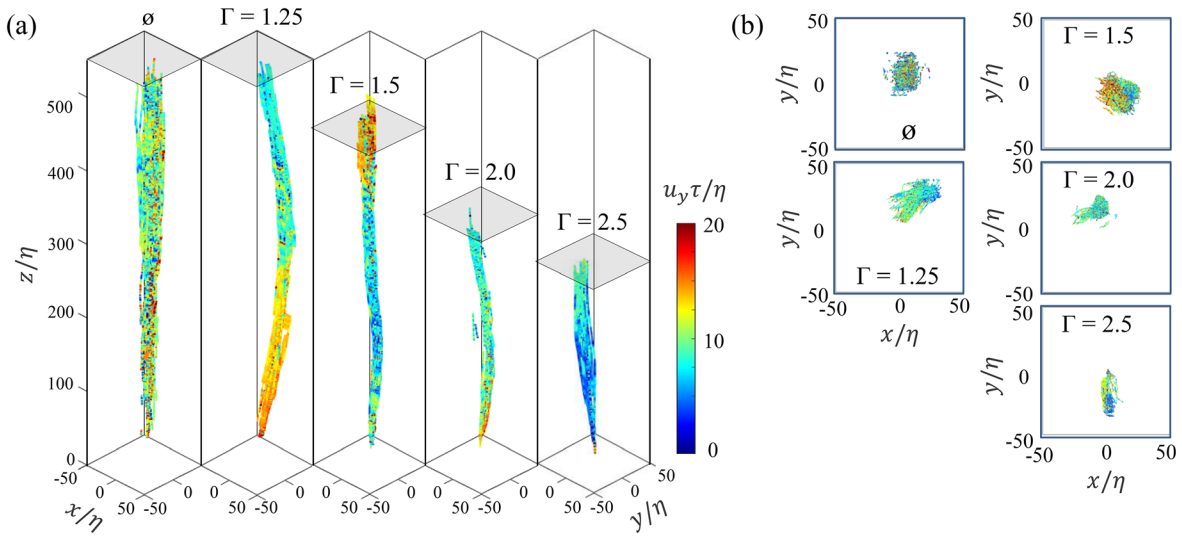

FIG. 2. (a) 3D bubble trajectories in a quiescent medium, ϕ, and convective flows at various aspect ratios, Γ. (b) Time history of the bubbles at an horizontal plane near the top. Colors show bubbles' lateral velocity, normalized by the Kolmogorov length and time scales.

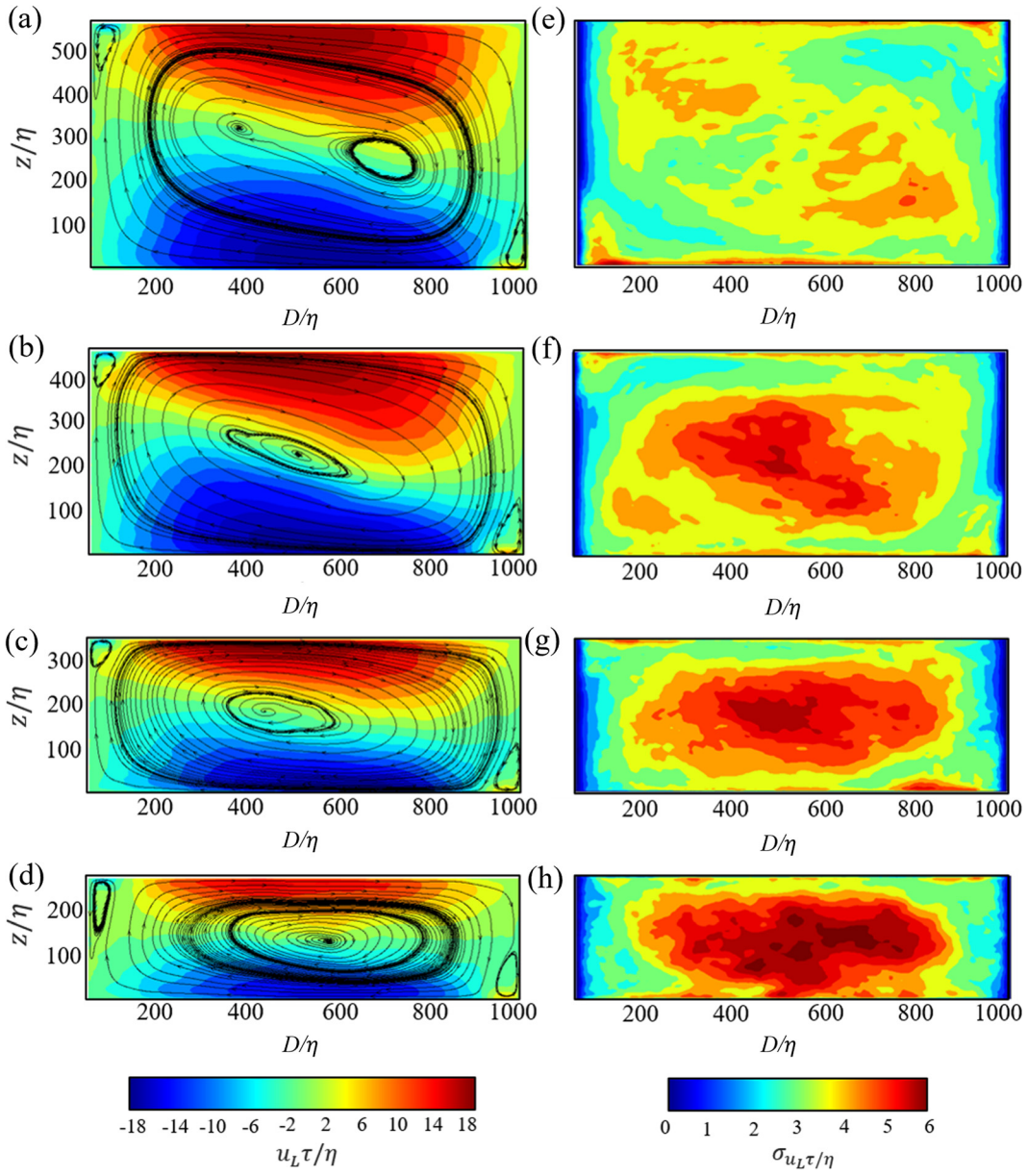

FIG. 3. In-plane velocity field and streamlines in the vertical diagonal plane of the RB box for Γ = (a) 1.25, (b) 1.5, (c) 2, and (d) 2.5; (e)–(h) standard deviations of the velocity fluctuations of the sub-figures at the left.

Distributions of the turbulent stresses along the vertical lines coincident with the location of the bubbles' release ($S/D = -1/2$ and 1/2) provide a quantitative assessment of the second-order statistics of the flow around the path of the bubbles and help us to understand quantities associated with the measured bubbles trajectories. Figures 4 and 5 show all the components of the Reynolds stress normalized by the Kolmogorov scales $(\tau/\eta)^2$, where the roll points upward ($S/D = -1/2$) and downward ($S/D = 1/2$). The level of the horizontal velocity fluctuations, $\langle u'u' \rangle$ and $\langle v'v' \rangle$, are comparatively larger than the vertical counterpart, $\langle w'w' \rangle$. The horizontal velocity fluctuations also exhibit larger dependence with aspect ratio with higher Γ inducing higher fluctuations across the vertical span and maximum values around the center and near the bottom and top walls. The turbulent shear stresses, $\langle u'v' \rangle$, $\langle u'w' \rangle$, and $\langle v'w' \rangle$ are clearly modulated by the aspect ratio, but their magnitudes are substantially lower than the normal components. Overall, the turbulent stress profiles do not show very significant differences between the two locations, indicating that the mean convective motion of the roll played a dominant role in the features of the bubbles motions.

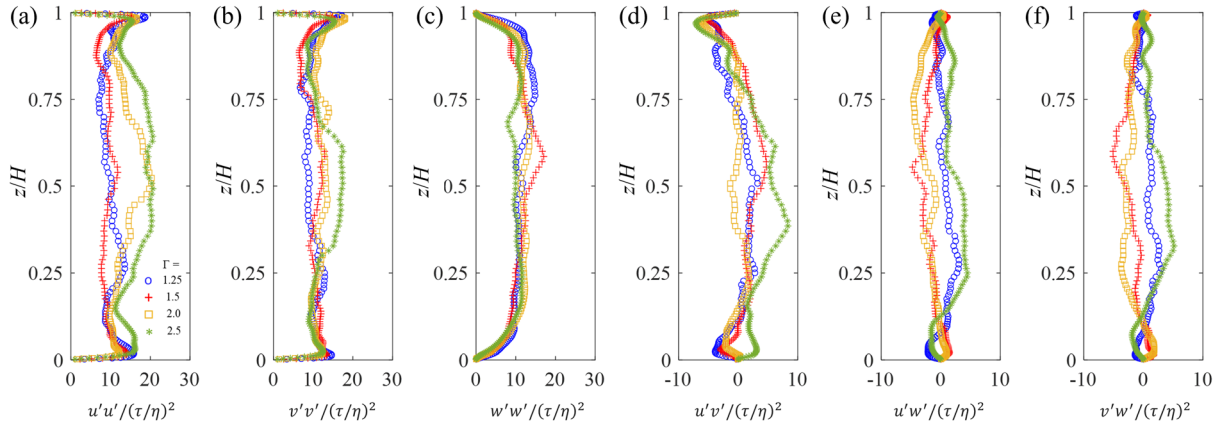

FIG. 4. Reynolds stress components along the vertical line coincident with on the bubble stream release at $s/D = -1/2$, where the roll points upward. (a) $\langle u'u' \rangle$, (b) $\langle v'v' \rangle$, (c) $\langle w'w' \rangle$, (d) $\langle u'v' \rangle$, (e) $\langle u'w' \rangle$, and (f) $\langle v'w' \rangle$. τ and η denote the Kolmogorov time and length scales, respectively.

Comparison of the measured and simulated mean y-axis velocity component, u_y, and associated standard deviation, σ_{u_y}, profiles with height, z/H, are shown in Fig. 6 for the various Γ. The mean velocity profiles normalized with Kolmogorov scales (τ/η) show a relatively good agreement between simulations and experiments. The deviations, particularly at high Γ, may indicate instability of the dominant roll structure at a high Γ.[16,29] Also, and similar to the work of Kim *et al.*,[11] numerical results of the standard deviation of the bubbles' lateral velocity are relatively underestimated due to the absence of two-way coupling on the simulations and distinct phenomena, including path instability of bubbles and the associated effect on the convective turbulence. In particular, path instability of a millimetric bubble has been known to aggravate in a turbulent environment according to Shim *et al.*[30] For all aspect ratios, the standard deviation of the bubbles lateral velocity shown in Fig. 6(b) indicates insensitivity to the aspect ratio in the current simulations, which is incapable of simulating path instability. However, the measured standard deviation exhibits quite irregular variation along the height, which might be due to the enhanced path instability of millimetric bubbles by turbulence.[30] Even the measured mean velocity shows wildly oscillatory behavior as shown in Fig. 6(a), more pronounced for $\Gamma = 1.5$ and 2, for which the measured standard deviation overestimates the simulation result. The coincidental agreement for $\Gamma = 2.5$ seems to be due to suppressed path instability in the experiment. The differences in these two quantities between measurements and simulations provide insight into the approximation of one-way vs two-way bubble coupling and sensitivity with aspect ratios.

A close look at the modulation of the aspect ratio on the characteristics of the bubble motions can be obtained with bulk features of the experimentally measured bubble streams. This includes, at a given height, the location of the center of mass of the bubbles, L_c, the mean lateral deviation of the bubbles with respect to the center of mass, R_c, the collective vertical, u_z, and lateral, u_L, velocity components, and the associated velocity ratio, u_z/u_L, which is a measure of the bubble stream expansion. These quantities are shown in Figs. 7 and 8 for the bubble streams at $s/D = -1/2$ and $s/D = 1/2$, respectively. They reveal remarkable features of the effects of the Γ-modulated roll structures. Indeed, the maximum mean deviation of the bubble stream

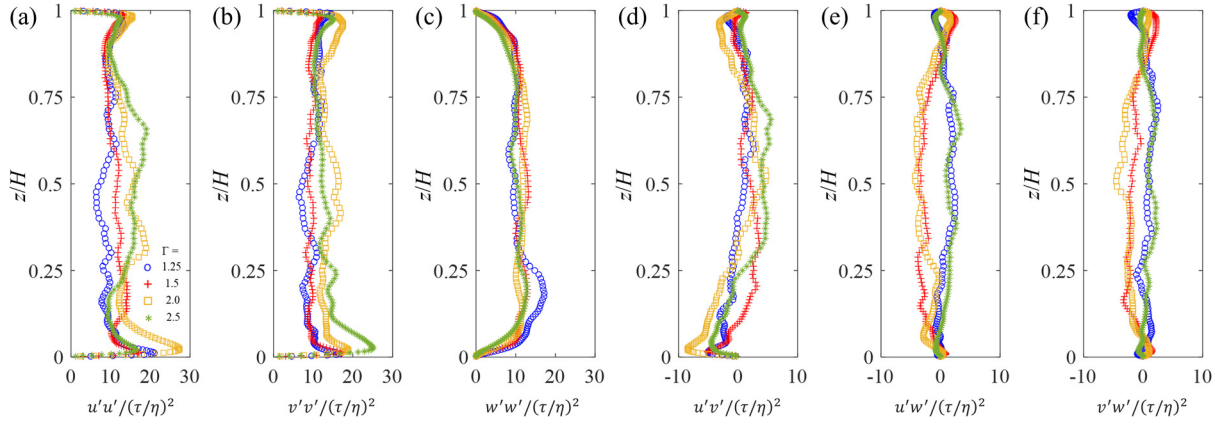

FIG. 5. Reynolds stress components along the vertical line coincident with on the bubble stream release at $s/D = 1/2$, where the roll points downward. (a) $\langle u'u' \rangle$, (b) $\langle v'v' \rangle$, (c) $\langle w'w' \rangle$, (d) $\langle u'v' \rangle$, (e) $\langle u'w' \rangle$, and (f) $\langle v'w' \rangle$. τ and η denote the Kolmogorov time and length scales, respectively.

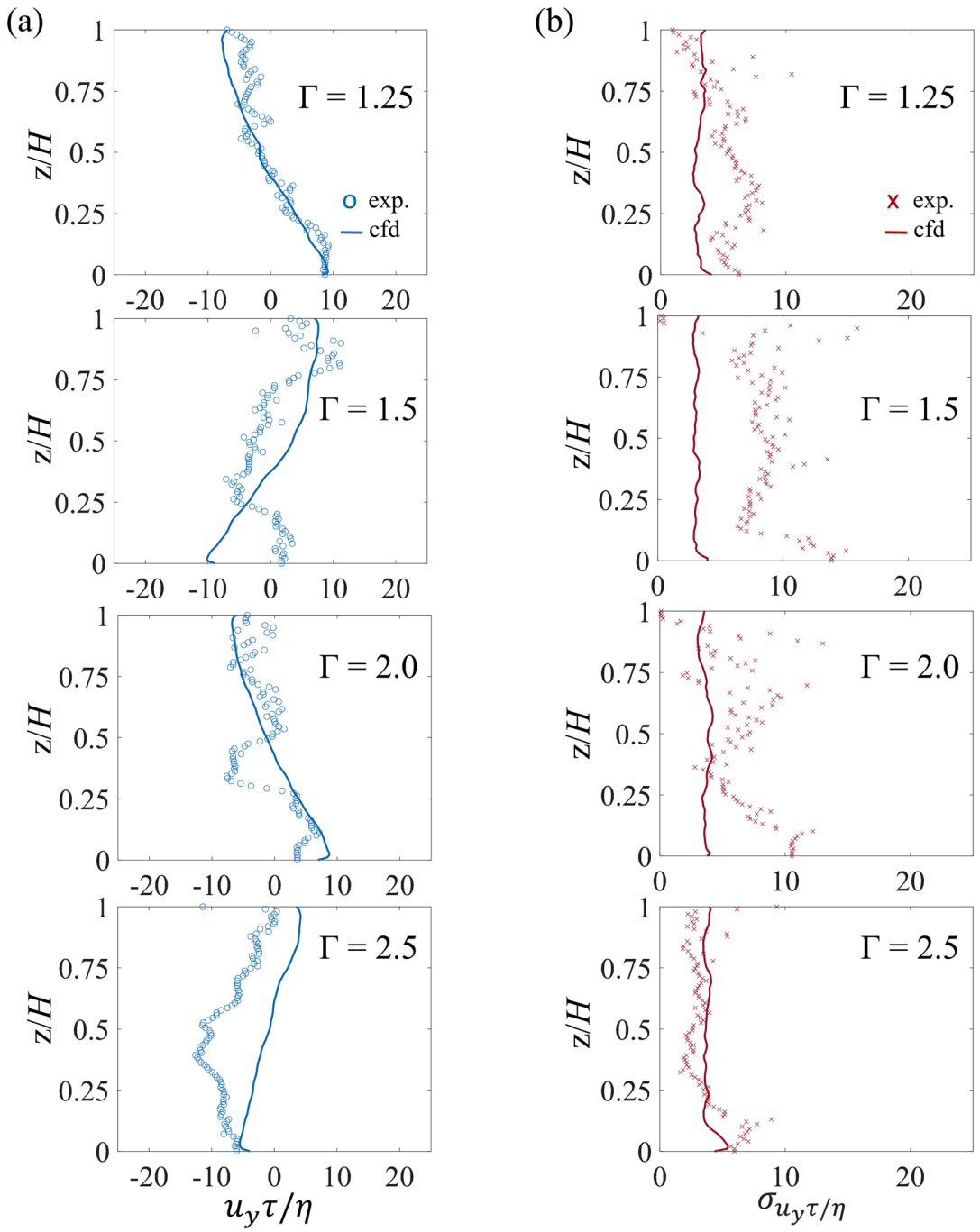

FIG. 6. Comparison of the (a) lateral velocity, u_y, and (b) standard deviations, σ_{u_y}, of the rising bubbles in the y-direction at various Γ. τ and η denote the Kolmogorov time and length scales, respectively.

occurred at half height in the scenario with the lowest aspect ratio ($\Gamma = 1.25$) for the $s/D = -1/2$ stream, where the roll contributed to the motion of the bubbles around the middle span; however, it was near the top in the highest Γ (=2.5). Note that the bulk mean deviation with respect to the center of mass, or bulk radius of the superimposed trajectories, increased with height. This is consistent with the roughly regular velocity ratio, u_z/u_L, across the vertical. It was on the order of 5–7, which indicates an angle of expansion with respect to the vertical of $\alpha = \tan^{-1}(u_z/u_L) \sim 8°$–$10°$. It is worth noting the effect of roll motion on the velocity of the bubbles; indeed,

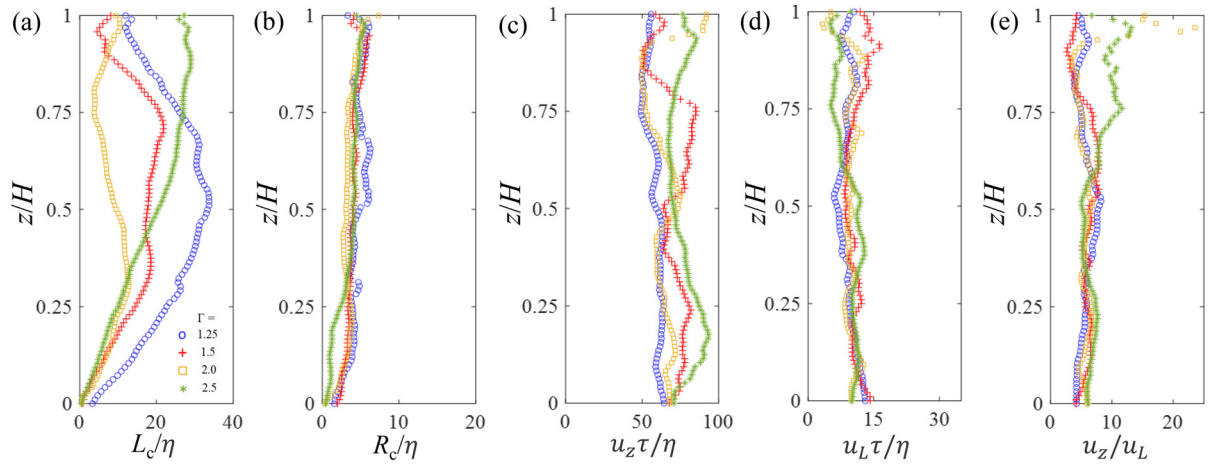

FIG. 7. Bulk features of the bubble stream at $s/D = -1/2$ for various Γ. (a) Bulk lateral distance (center of mass, L_c); (b) mean lateral deviation with respect to the center of mass, R_c; (c) vertical, v_z, and (d) lateral v_L velocity components; (e) velocity ratio, v_z/v_L.

bubbles roughly rose with $u_z\tau/\eta \sim 60$–80 when the flow (roll) moved upward; however, $u_z\tau/\eta \sim 50$ in the case roll motions opposed to the bubbles. Also, in this case, Γ did not substantially affect u_z. However, this was not the case in the scenarios with the roll contributing to the bubble motions; comparatively, higher velocity occurred at the highest aspect ratio. It is worth stressing the dominant effect of the relative motion of the roll with respect to the bubbles mean deviation, R_c. As pointed out, the turbulent stresses along the vertical lines at $s/D = -1/2$ and $s/D = 1/2$ did not differ substantially (see Figs. 4 and 5); however, the mean bubble deviation showed large differences at the two s/D locations. This quantity exhibited regular trends with weak dependence with Γ at $s/D = -1/2$, i.e., where the roll roughly moved in with the bubbles. In contrast, R_c showed irregular, Γ−dependent patterns at $s/D = 1/2$, i.e., where the roll roughly moved against the bubbles.

Quantification of the pair dispersion, R^2, of the rising bubbles in the various convective flow scenarios and comparison with the base case (quiescent medium) contributes to uncovering distinct dynamics of the bubbles and the effect of the aspect ratio. In particular, the vertical component of the pair dispersion, R_z^2, is illustrated in Fig. 9. This quantity was not affected by the aspect ratio, showing a consistent temporal power-law dependence $R_z^2 \propto t^2$ regardless of Γ [Fig. 9(a)]. It indicates that the vertical pair dispersion is mainly influenced by the buoyancy rather than the convective motion.[11] However, the lateral pair dispersion in the y-direction, R_L^2 following Ref. 11, shows distinct characteristics with respect to Γ [Fig. 9(b)]. As Γ increases, the magnitude of lateral pair dispersion decreases while the bulk behavior follows $R_L^2 \propto t^{3/2}$ regardless of Γ at the ballistic regime $t/\tau < 1$. However, in the diffusive regime $t/\tau > 1$, the dispersion rate decreases as Γ increases. It is worth noting that in the case of $\Gamma = 2.5$, the pair

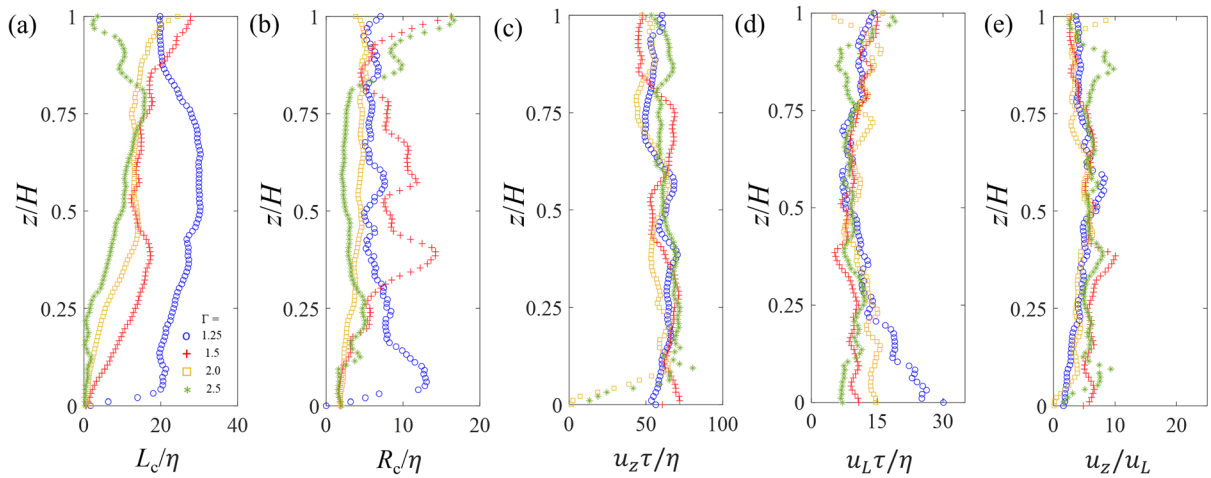

FIG. 8. Bulk features of the bubble stream at $s/D = 1/2$ for various Γ. (a) Bulk lateral distance (center of mass, L_c); (b) mean lateral deviation with respect to the center of mass, R_c; (c) vertical, v_z, and (d) lateral v_L velocity components; (e) velocity ratio, v_z/v_L.

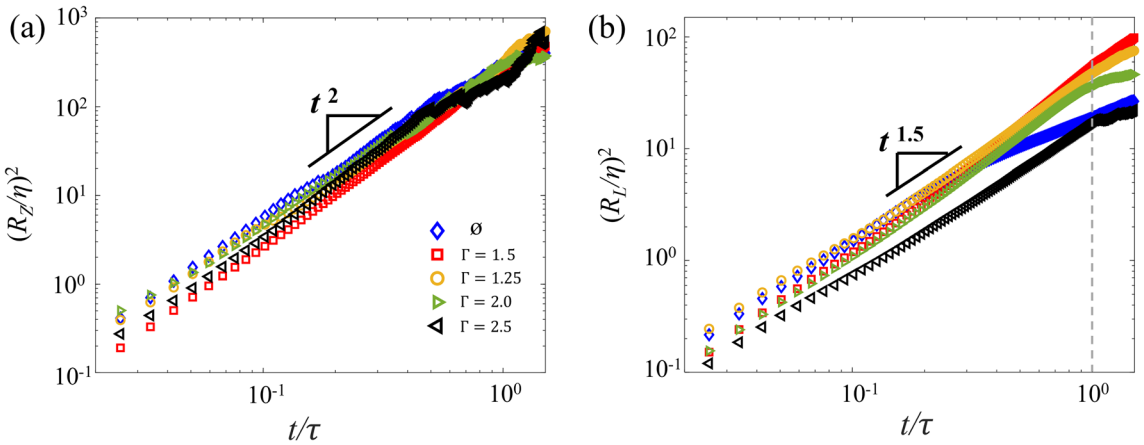

FIG. 9. (a) Vertical (R_z^2) and (b) lateral (R_L^2) non-dimensional pair dispersion in the convective flows at different aspect ratios, Γ.

dispersion at the diffusive regime nearly collapses with that of the quiescent medium. It shows that at a high Γ, the comparatively reduced roll structure has a minor effect on the bulk dispersion in the diffusive regime.

The lateral pair dispersion, R_L^2 over a wide range of initial separations $r_p/H = 1/10$, 2/10, 3/10, 4/10, and $5H/10$ is illustrated in Fig. 10 to further highlight various phenomena. For all aspect ratios, the lateral pair dispersion tended to increase faster with larger initial separations. This trend is particularly evident at $\Gamma = 1.25$, compared to other cases. In addition, the pair dispersion at a large initial separation, for example, $r > 4H/10$, is affected by the overall convective roll structure, showing a clear trend with respect to the aspect ratio. As Γ increases, the pair dispersion decreases, particularly at large separation times, $t/\tau > 1$. Finally, it is worth highlighting that the lateral pair dispersion exhibits a clear trend with respect to the aspect ratio when the initial separation is larger than $4H/10$, see Fig. 11 for selected instants. It decreased as the aspect ratio increased, particularly, near the transition regime $t/\tau \sim 1$.

IV. CONCLUSIONS

We have experimentally and numerically explored and characterized the dynamics of air bubbles in Rayleigh–Bénard convection at various aspect ratios of $\Gamma = 1.25$, 1.5, 2, and 2.5 under Rayleigh numbers ranging from 2.0×10^9 to 1.6×10^{10} with similar Kolmogorov microscales. The characterization of the bulk features of the superimposed bubble trajectories using the center of mass, mean deviation, vertical and lateral velocities, and their ratios allowed one to capture distinct modulation of the roll structure and, consequently, Γ. In particular, these quantities showed the effect of the motion direction of the convective roll in the velocity of the bubbles, and stream expansion. Also, they provide a simple view of the effect of Γ on the mean bubbles' trajectories. The aspect ratio showed a minor effect on the vertical pair dispersion of the rising bubbles, where the buoyancy dominates over the convective motion. However, the lateral pair dispersion showed correlated trends with the aspect ratio, particularly at large initial separations and times. As the aspect ratio increased, the magnitude of dispersion decreased. It indicates the effect of the different-sized roll structures modulated by the aspect ratio. Pair dispersion as a function of the aspect ratio at various initial separation and time further highlights the bubble dynamics in RB convection at different aspect ratios. Future work will include an investigation of bubble dynamics with the coexistence of multi-roll structures and non-canonical RB convection.

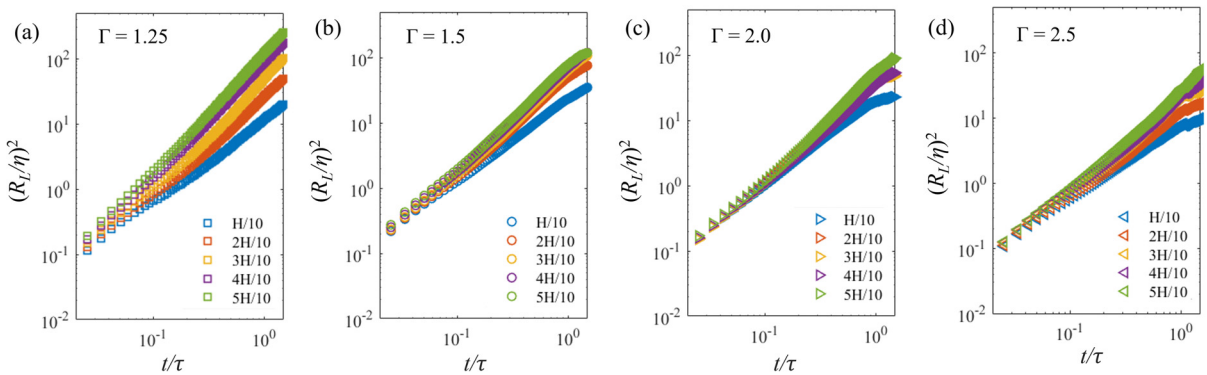

FIG. 10. Dimensionless lateral pair dispersion in the *y*-direction for various initial separations, *r*, ranging from $H/10$ to $5H/10$ for $\Gamma =$ (a) 1.25, (b) 1.5, (c) 2.0, and (d) 2.5.

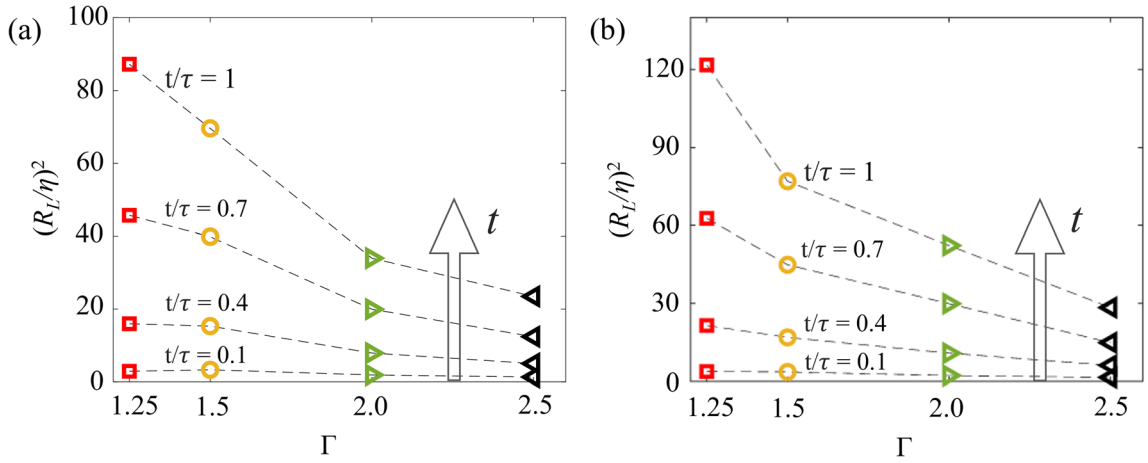

FIG. 11. Dimensionless lateral pair dispersion in the lateral direction with respect to the aspect ratio for the initial separation (a) $4H/10$ and (b) $5H/10$ at selected instants.

ACKNOWLEDGMENTS

This research was funded by the National Science Foundation, Grant No. CBET-1912824. The work by C.L. was supported by Samsung Science and Technology Foundation (No. SSTF-BA1702_03).

DATA AVAILABILITY

The data that support the findings of this study are available from the corresponding author upon reasonable request.

REFERENCES

[1]E. Bodenschatz, W. Pesch, and G. Ahlers, "Recent developments in Rayleigh–Bénard convection," Annu. Rev. Fluid Mech. **32**, 709–778 (2000).
[2]F. Toschi and E. Bodenschatz, "Lagrangian properties of particles in turbulence," Annu. Rev. Fluid Mech. **41**, 375–404 (2009).
[3]J. Salazar and L. Collins, "Two-particle dispersion in isotropic turbulent flows," Annu. Rev. Fluid Mech. **41**, 405–432 (2009).
[4]O. Liot, A. Gay, J. Salort, M. Bourgoin, and F. Chillà, "Inhomogeneity and lagrangian unsteadiness in turbulent thermal convection," Phys. Rev. Fluids **1**, 064406 (2016).
[5]X.-M. Li, S.-D. Huang, R. Ni, and K.-Q. Xia, "Lagrangian velocity and acceleration measurements in plume-rich regions of turbulent Rayleigh–Bénard convection," Phys. Rev. Fluids **6**, 053503 (2021).
[6]J. Schumacher, "Lagrangian dispersion and heat transport in convective turbulence," Phys. Rev. Lett. **100**, 134502 (2008).
[7]R. Ni, S.-D. Huang, and K.-Q. Xia, "Lagrangian acceleration measurements in convective thermal turbulence," J. Fluid Mech. **692**, 395–419 (2012).
[8]J.-T. Kim, S. Shen, S. DiMarco, Y. Jin, and L. Chamorro, "Lagrangian acceleration in Rayleigh–Bénard convection at various aspect ratios," Phys. Rev. Fluids **3**, 113502 (2018).
[9]C. Schneide, A. Pandey, K. Padberg-Gehle, and J. Schumacher, "Probing turbulent superstructures in Rayleigh–Bénard convection by Lagrangian trajectory clusters," Phys. Rev. Fluids **3**, 113501 (2018).
[10]O. Liot, D. Martin-Calle, A. Gay, J. Salort, F. Chillà, and M. Bourgoin, "Pair dispersion in inhomogeneous turbulent thermal convection," Phys. Rev. Fluids **4**, 094603 (2019).
[11]J.-T. Kim, J. Nam, S. Shen, C. Lee, and L. Chamorro, "On the dynamics of air bubbles in Rayleigh–Bénard convection," J. Fluid Mech. **891**, A7 (2020).
[12]M. Maxey, "The gravitational settling of aerosol particles in homogeneous turbulence and random flow fields," J. Fluid Mech. **174**, 441–465 (1987).
[13]E. Balkovsky, G. Falkovich, and A. Fouxon, "Intermittent distribution of inertial particles in turbulent flows," Phys. Rev. Lett. **86**, 2790–2793 (2001).
[14]M. Calzavarini, E. Cencini, D. Lohse, and F. Toschi (International Collaboration for Turbulence Research), "Quantifying turbulence-induced segregation of inertial particles," Phys. Rev. Lett. **101**, 084504 (2008).
[15]V. Mathai, S. Huisman, C. Sun, D. Lohse, and M. Bourgoin, "Dispersion of air bubbles in isotropic turbulence," Phys. Rev. Lett. **121**, 054501 (2018).
[16]J. Bailon-Cuba, M. S. Emran, and J. Schumacher, "Aspect ratio dependence of heat transfer and large-scale flow in turbulent convection," J. Fluid Mech. **655**, 152–173 (2010).
[17]S.-D. Huang, M. Kaczorowski, R. Ni, K.-Q. Xia *et al.*, "Confinement-induced heat-transport enhancement in turbulent thermal convection," Phys. Rev. Lett. **111**, 104501 (2013).
[18]X.-J. Huang, Y.-P. Hu, and Y.-R. Li, "Aspect ratio dependence of Rayleigh–Bénard convection of cold water near its maximum density in box-shaped containers," Phys. Fluids **31**, 075107 (2019).
[19]H.-D. Xi and K.-Q. Xia, "Cessations and reversals of the large-scale circulation in turbulent thermal convection," Phys. Rev. E **75**, 066307 (2007).
[20]R. Ni, S.-D. Huang, and K.-Q. Xia, "Reversals of the large-scale circulation in quasi-2d Rayleigh–Bénard convection," J. Fluid Mech. **778**, R5 (2015).
[21]S.-D. Huang and K.-Q. Xia, "Effects of geometric confinement in quasi-2-d turbulent Rayleigh–Bénard convection," J. Fluid Mech. **794**, 639–654 (2016).
[22]S. Elghobashi, "On predicting particle-laden turbulent flows," Appl. Sci. Res. **52**, 309–329 (1994).
[23]F. Luetteke, X. Zhang, and J. Franke, "Implementation of the Hungarian method for object tracking on a camera monitored transportation system," in *ROBOTIK 2012; 7th German Conference on Robotics*, Munich (WikiCFP, 2012), pp. 343–348.
[24]M. Rai and P. Moin, "Direct simulations of turbulent flow using finite-difference schemes," J. Comput. Phys. **96**, 15–53 (1991).
[25]I. Mazzitelli, D. Lohse, and F. Toschi, "On the relevance of the lift force in bubbly turbulence," J. Fluid Mech. **488**, 283 (2003).
[26]I. Fouxon, G. Shim, S. Lee, and C. Lee, "Multifractality of fine bubbles in turbulence due to lift," Phys. Rev. Fluids **3**, 124305 (2018).
[27]G. Shim, H. Park, S. Lee, and C. Lee, "Behavior of microbubbles in homogeneous stratified turbulence," Phys. Rev. Fluids **5**, 074302 (2020).
[28]H. Shim and C. Lee, "Two-way interaction between isotropic turbulence and dispersed bubbles," J. Mech. Sci. Technol. **35**, 1527–1537 (2021).
[29]L. Zwirner, A. Tilgner, and O. Shishkina, "Elliptical instability and multiple-roll flow modes of the large-scale circulation in confined turbulent Rayleigh–Bénard convection," Phys. Rev. Lett. **125**, 054502 (2020).
[30]G. Shim, J. Kim, and C. Lee, "Path instability of a no-slip spheroidal bubble in isotropic turbulence," Phys. Rev. Fluids **6**, 073603 (2021).